

Imaging with LINC-NIRVANA, the Fizeau interferometer of the Large Binocular Telescope:
state of the art and open problems

This article has been downloaded from IOPscience. Please scroll down to see the full text article.

2011 Inverse Problems 27 113001

(<http://iopscience.iop.org/0266-5611/27/11/113001>)

View [the table of contents for this issue](#), or go to the [journal homepage](#) for more

Download details:

IP Address: 130.251.61.251

The article was downloaded on 17/11/2011 at 09:40

Please note that [terms and conditions apply](#).

TOPICAL REVIEW

Imaging with LINC-NIRVANA, the Fizeau interferometer of the Large Binocular Telescope: state of the art and open problems

M Bertero¹, P Boccacci¹, A La Camera¹, C Olivieri¹ and M Carbillet²

¹ Dipartimento di Informatica e Scienze dell'Informazione, Università di Genova,
Via Dodecaneso 35, 16146 Genova, Italy

² UMR 6525 H. Fizeau, Université de Nice Sophia Antipolis/CNRS/Observatoire de la Côte
d'Azur, Parc Valrose, 06108 Nice cedex 2, France

E-mail: bertero@disi.unige.it

Received 29 July 2011

Published 28 October 2011

Online at stacks.iop.org/IP/27/113001

Abstract

LINC-NIRVANA (LN) is the Fizeau interferometer of the Large Binocular Telescope which consists of two 8.4 m mirrors with a center-to-center distance of 14.4 m, hence providing a maximum path of 22.8 m in the direction of the baseline joining the two centers. LN is a true imager since interference occurs in the focal plane and not in the aperture plane as with essentially all the existing interferometers. However, an LN image is characterized by an anisotropic resolution: that of a 22.8 m mirror in the direction of the baseline and that of a 8.4 m mirror in the orthogonal direction. In order to obtain a unique image with a high and isotropic resolution, several images must be detected with different orientations of the baseline and suitably processed. Therefore, the instrument will routinely require the use of image reconstruction methods for providing astronomical images with unprecedented resolution, in principle ten times the resolution of the Hubble Space Telescope. This review concerns the image reconstruction problem for LN and is based essentially on our work. After a description of the main features of the telescope and of the interferometer, it contains a discussion of the problem and of the approximations introduced in its formulation. In short, it is reduced to multiple-image deconvolution with Poisson data. Similarity with the image reconstruction problem in emission tomography is stressed and utilized for introducing suitable iterative reconstruction methods. These methods are extended to regularized versions of the problem. Efficiency is another important issue because the size of LN images is of the order of 4.2 megapixels; therefore, acceleration methods are also discussed. All methods are tested on synthetic images because, even if the instrument is in an advanced stage of realization, it will be presumably operative in 2014. The algorithms of the proposed image reconstruction methods are

implemented in the Software Package AIRY (astronomical image restoration in interferometry), which can be downloaded from <http://www.airyproject.eu>. AIRY is designed for simulation and subsequent reconstruction of LN images. A discussion of the several specific problems that must still be solved for obtaining accurate and efficient reconstructions is inserted at the end of this review.

1. Introduction

The Large Binocular Telescope (LBT), originally called the Columbus Project Telescope and jointly conceived at the end of the eighties by people of the University of Arizona and Osservatorio Astrofisico di Arcetri, is now an international collaboration among institutions in the United States, Italy and Germany (<http://www.lbto.org>). The LBT Corporation partners are the University of Arizona on behalf of the Arizona University system; Istituto Nazionale di Astrofisica, Italy; LBT Beteiligungsgesellschaft, Germany, representing the Max Planck Society, the Astrophysical Institute Potsdam and Heidelberg University; Ohio State University; Research Corporation, on behalf of the University of Notre Dame, University of Minnesota and University of Virginia.

The telescope is located at about 3300 m on Mount Graham, AZ. The choice of location caused considerable controversy from environmentalists and the San Carlos Apache Tribe, who claimed that the mountain is sacred. Even if not all the instruments are already operative, LBT has produced the first outstanding results.

Indeed it is a very innovative telescope, consisting of two 8.4 m primary mirrors on the same alt-azimuth mount with a center-to-center distance of 14.4 m and one of the two mirrors is already equipped with the best existing adaptive optics (AO) system. Moreover, the particular structure of LBT allows observation modes not possible with traditional telescopes. One of these modes, which is the main motivation of this review, is based on Fizeau interferometry thanks to an instrument called LINC-NIRVANA (Lbt INterferometric Camera and Near-InfraRed/Visible Adaptive iNterferometer for Astronomy) (<http://www.mpia.de/LINC/>). It will provide images with unprecedented resolution, theoretically ten times higher than that of the Hubble Space Telescope (HST). From the point of view of researchers in image processing, the interesting feature of this instrument is that for reaching such a resolution, it will routinely require the use of both accurate and efficient image reconstruction methods (the size of the images will be of the order of 4.2 megapixels). The underlying image reconstruction problem can be modeled as a multiple image deconvolution, with some similarity to image reconstruction from projections in tomography.

The first simulations, aiming to demonstrate the possibility of reaching the resolution of a 22.8 m telescope by means of Fizeau interferometry applied to LBT, were based on the extension of a physically constrained iterative deconvolution algorithm [34, 35] (see also <http://www.lbto.org/why.htm>). One year later, another approach, based on the assumption of data Poisson statistics and on the adaptation of methods used in emission tomography, was proposed and tested on a few synthetic images [10, 11]. Single-image deconvolution methods were investigated in [37] by considering a co-adding of the different interferometric images, while a different reduction of the multiple images to a single one was proposed in [61] under the assumption of additive Gaussian noise.

This review is essentially based on our work and is a survey of the methods we proposed, of their validation and of the many open problems that will become crucial when the instrument will be operative. The algorithms of the methods described in this review are implemented in the Software Package AIRY (Astronomical Image Restoration in interferometrY) [24], designed for the simulation and reconstruction of interferometric images. The software can be downloaded from <http://www.airyproject.eu>.

The review is organized as follows. We first give a brief description of LBT and of the interferometer LINC-NIRVANA (LN), focusing on the specific features of the images provided by this instrument and the specific preprocessing which is required for subsequent deconvolution. Next we discuss the image reconstruction problem, analyzing the different kinds of noise affecting the images and formulating both maximum likelihood and Bayesian (or regularization) approaches. The important question of the choice of the regularization parameter is also briefly discussed. Iterative algorithms for the different approaches are introduced, also discussing their modifications for boundary effects correction and efficiency improvement. The last part is devoted to the illustration of several numerical experiments intended to demonstrate results achievable by means of the proposed methods. A summary of open problems concludes the review.

2. The Large Binocular Telescope Observatory

The Large Binocular Telescope Observatory (LBTO) is a part of the Mount Graham International Observatory, consisting also of the Vatican Advanced Technology Telescope and the Heinrich Hertz Submillimeter Telescope. LBTO hosts LBT and its very innovative instrumentation.

2.1. The LBT

The LBT is the world's largest optical and infrared telescope since it consists of two 8.4 m primary mirrors with the total light-gathering power of a single 11.8 m telescope. The two mirrors have an elevation over an azimuth mounting and the elevation optical support structure moves on two large C-shaped rings (see figure 1). They are mounted with a 14.4 m center separation, hence with an edge-to-edge distance of 22.8 m. This particular structure makes Fizeau interferometry possible, described in the next subsection, with a maximum baseline of 22.8 m, corresponding to a theoretical resolution of a 22.8 m mirror in the direction of the line joining the two centers.

Two instruments are currently available at the LBT: the Large Binocular Camera (LBC), made of two optical cameras located at the prime focus station of the two mirrors, and LUCIFER (LUCI, for short), a near-infrared imager/spectrograph. The LBC is a wide-field seeing-limited imager: the left camera (see figure 1) is optimized for UV-blue wavelengths and the other one for red-IR wavelengths. Each camera has a field of view (FoV) equivalent to $23' \times 23'$ with a pixel size of about $0.23''$, adequate to match the best seeing conditions. LUCI is the near-infrared instrument for LBT, operating in the band $0.9\text{--}2.5 \mu\text{m}$, with a 2048×2048 pixel camera, and provides imaging and spectroscopic capabilities in seeing- and diffraction-limited modes. LUCI1 is available for (seeing-limited) science investigation on the right mirror of LBT.

The first light of the telescope was obtained during the night of 12 October 2005 with the blue LBC camera while the first binocular light was obtained during the night of 6 March 2008 using both LBC cameras. The images obtained, shown in figure 2, demonstrate the first

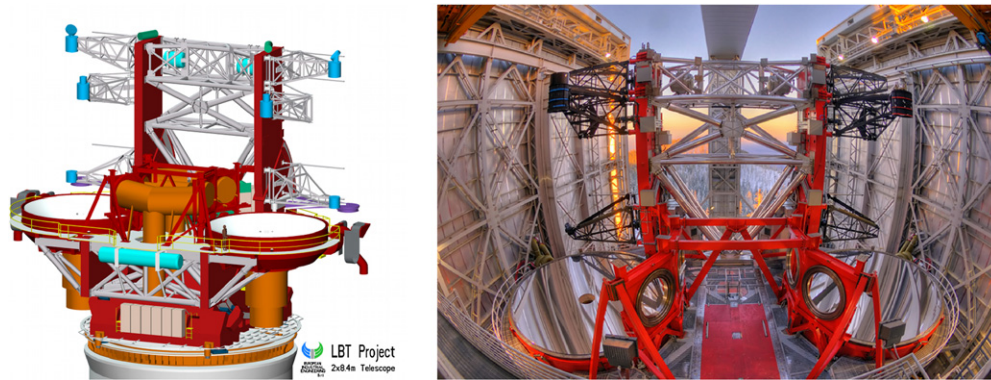


Figure 1. A design view of LBT (left), and a fish-eye image of the same side of LBT inside the enclosure (right), as it appears to the visitors of the observatory (photo courtesy of Ruyopakam and the LBTO). The left side of these pictures corresponds to the left side of the telescope mentioned in the text.

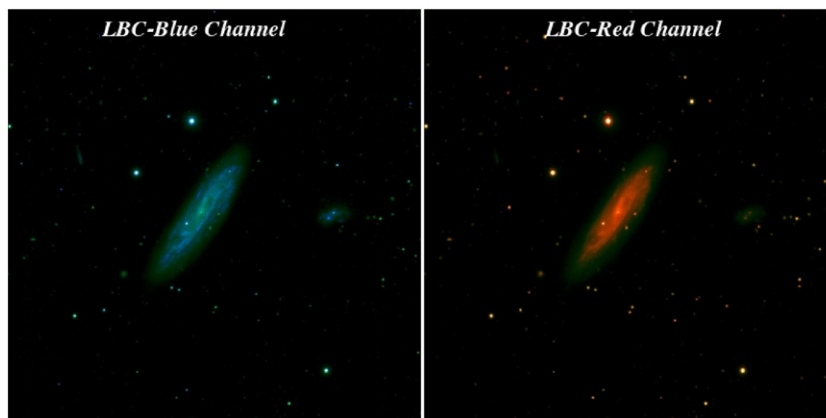


Figure 2. First binocular light of the galaxy NGC2770, obtained in the night of 6 March 2008 with LBC (photo courtesy of the LBC Team and the Large Binocular Observatory).

innovative feature of LBT, namely the possibility of observing simultaneously the same target at different wavelengths.

The AO system of the telescope is also very innovative [29]. Designed by the Arcetri Observatory and developed within a collaboration between Italian INAF and the University of Arizona, it consists of deformable secondary mirrors and therefore does not require additional optical elements. Each mirror has a diameter of 0.91 m and is deformed by 672 actuators. Moreover, pyramid wave-front sensors are used. It uses natural guide stars and is called the First Light Adaptive Optics (FLAO) system.

The first adaptive secondary unit was mounted on the left side of the telescope and commissioning started on 26 May 2010. FLAO immediately outperformed all other comparable systems, achieving peak Strehl ratios (SR) of 80–84% in the H band, against the SR of 30–50% of the other major telescopes in the same band of near-infrared wavelengths. An impressive demonstration of the capabilities of this system is shown in figure 3 where the

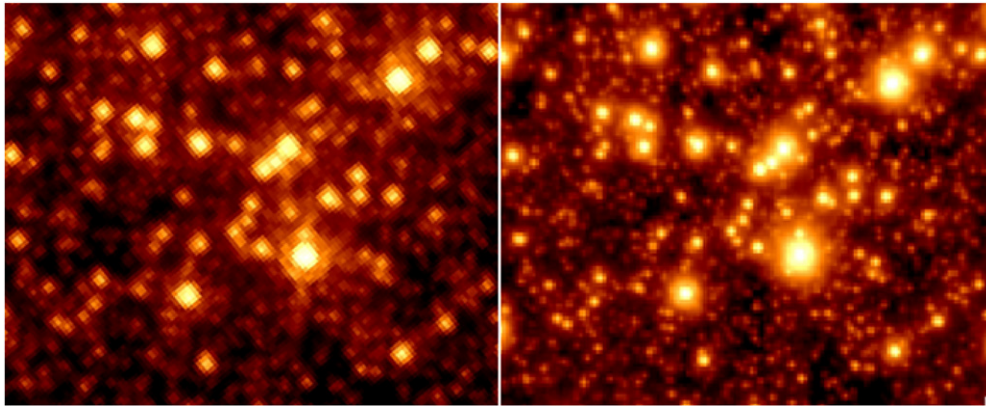


Figure 3. A central region of the globular cluster M92 at $1.6 \mu\text{m}$ as observed with HST (left) and with the FLAO system of LBT (right) (photo courtesy of the FLAO team and the LBTO).

image of a globular cluster provided by the HST is shown together with the image of the same target provided by the AO system of the LBT. It is clear that the resolution and depth achieved with LBT surpasses those of the Hubble image.

2.2. The interferometer LN

The LBT observing instruments split into two classes: instruments receiving light from one primary mirror only and instruments combining the beams of the two mirrors (interferometers). Two interferometers are planned for LBT: the Large Binocular Telescope Interferometer (LBTI) and LN. The LBTI is based on nulling and Fizeau interferometry for exploring regions surrounding nearby star systems for dust and planets; LN is also a Fizeau interferometer and will operate as a true imager since, in the Fizeau mode, the two beams from the primary mirrors are combined in a common focal plane (not in the pupil plane as with essentially all the existing interferometers).

LN [36, 51] is in an advanced realization phase by a consortium of German and Italian institutions, led by the Max Planck Institute for Astronomy in Heidelberg. When completed, the instrument will be mounted in the center of the platform of LBT (clearly visible in the right panel of figure 1), immediately adjacent to LBTI. It will be fully commissioned and available for scientific studies in 2014.

LN will be equipped with a HAWAII-2 detector consisting of 2048×2048 pixels with a pixel size of about 5 mas, thus producing for each orientation of the baseline a raw image of 4.2 megapixels with a FoV of $10'' \times 10''$. The detector will work in the range $1.0\text{--}2.4 \mu\text{m}$, providing an oversampling by a factor 4 in the K-band ($2.2 \mu\text{m}$) since the diffraction limit of a 22.8 m telescope in this band is about 20 mas.

In figure 4, we show a simulated point spread function (PSF) with $\text{SR} = 70\%$, together with the corresponding modular transfer function (MTF), i.e. the modulus of the Fourier transform of the PSF. This PSF, as well as the others used in this review, has been obtained with the code LOST [7]. It is monochromatic ($\lambda = 2.2 \mu\text{m}$, i.e. the K band) and not affected by the smearing effect discussed in section 3.1. As clearly appears from this figure, it is the PSF of a 8.4 m telescope modulated by the interferometric fringes; accordingly, in the MTF, the central disk corresponds to the band of a 8.4 m mirror while the two side disks

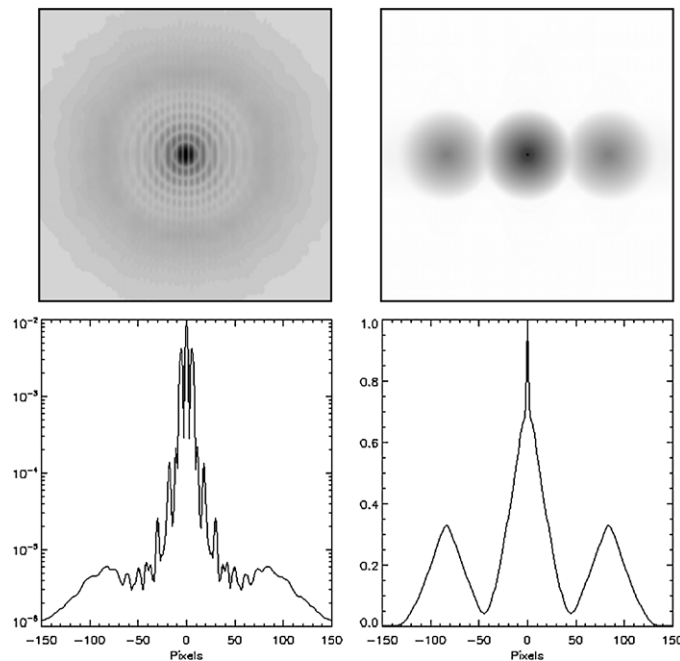


Figure 4. Simulated PSF of LN with $SR = 70\%$ (upper-left panel), and the corresponding MTF (upper-right panel), both represented with the reversed gray scale. The fringes are orthogonal to the baseline. In the lower panels, we show the cut of the PSF along the baseline (left) and the cut of the MTF along the same direction (right). In the image and in the cut of the PSF, the domain of AO correction is evident, as well as the beginning of the halo due to the residual seeing effect.

are replicas due to interferometry, with a weaker intensity than the central one. These disks contain the precious additional information on the target due to interferometry. We also stress that, as follows from this analysis, LN images will be characterized by an anisotropic resolution: that of a 22.8 m telescope in the direction of the baseline, and that of a 8.4 m in the orthogonal direction. Therefore, in order to get the maximum resolution in all directions, it will be necessary to acquire different images of the same target with different orientations of the baseline and to combine these images into a unique high-resolution image by means of suitable image reconstruction methods. In other words, the LN will routinely require multiple-image deconvolution. We point out the similarity of this procedure with tomography, one LN image corresponding to one projection in tomography.

3. Image preprocessing

A standard preprocessing of the raw images, consisting in correction for the flat field, bad pixels, etc, must be performed. Moreover, the background due to sky emission and dark current must be estimated but not subtracted from the images; its estimated values are one of the inputs of the reconstruction algorithms. We do not describe this preprocessing, which is standard in astronomy. We focus on two non-standard operations that must be performed on LN images: de-rotation and PSF extraction.

3.1. Image de-rotation

During the integration (acquisition) time, the telescope must perform an altitude-azimuth motion for tracking the scientific target whose position is changing in the sky as a consequence of the Earth's rotation. Without correction, the field rotates while the fringes are fixed and orthogonal to the baseline. However, the FoV must be kept fixed and this can be obtained by a de-rotation system. As a result the fringes of the PSF rotate and a smearing of the PSF is produced (this effect is not shown in figure 4). It is obvious that the smearing cannot be too large otherwise it can produce a loss of resolution. Therefore, the de-rotation angle cannot be too large, let us say about 5° , corresponding to an integration time, in average, of 15 min. At the end of the acquisition, the instrument must be re-aligned with the baseline before acquiring another image with a different orientation of the baseline. In conclusion, all the different images of LN have the fringes in the same direction (conventionally the vertical one), with a moderate smearing, while the scientific target is located in different rotated positions inside the FoV. In each image, the rotation angle is given by the angle between its baseline and that of a reference image, for instance, the first acquired one.

The previous remarks imply that if we wish to have the same location of the target in all of the acquired images, we must de-rotate these images by means of suitable numerical algorithms. Several routines for image rotation exist in the available libraries (for instance, the ROT routine in the IDL library, frequently used by astronomers). They may produce artifacts and, for this reason, sometimes it may be convenient to de-rotate in the Fourier space rather than in the physical space [41]. We point out that each de-rotated image is contained in a broader array and that different images can contain different parts of the scientific object. This point will be briefly discussed in the following. However, if the angular size of the scientific object is significantly smaller than $10''$, then, from each de-rotated image, one can extract a squared patch containing only the object of interest.

3.2. PSF extraction

A modeling of the PSF corresponding to a given observation with LN is quite difficult, maybe impossible. Indeed, even the best AO system provides a correction only inside a limited region, depending on the distance between the actuators; outside this region, the PSF is still very significant and its behavior depends on the state of the atmosphere during the integration time (seeing). This effect is evident in figure 4.

It is possible to obtain information on the PSF if one or more stars are present in the FoV of the detector since the image of a star is basically the PSF of the instrument. In such a case, for each star, one can identify a region where the influence of the surrounding objects is not very important and extract a patch corresponding to this region. Of course the result is affected by background and noise and therefore a suitable processing and denoising of the extracted star image can be required [41]. The estimates of the PSF obtained in such a way have a much smaller size than the full image. An extension by zero padding is not convenient because the Fourier transform of the result has a band much broader than that of the instrument. Moreover, the halo of the PSF due to the seeing is important in the deconvolution of the detected images [23]. Therefore, it is necessary to extrapolate the extracted PSF with a function that can roughly simulate the seeing effect. Such a model is provided by a suitable Lorentz or, more generally, Moffat function, i.e. the following function of the angles $\{\phi_1, \phi_2\}$ in the sky:

$$\mathcal{M}(\phi) = \frac{a}{(1 + a_1\phi_1^2 + a_2\phi_2^2)^\beta}, \quad (1)$$

where a , a_1 , a_2 and β are parameters to be estimated. For a given β , the parameters a , a_1 , a_2 are obtained with a suitable fitting procedure (for details, see [41, 23]). Then, a crucial point is the estimation of β [23]. The solution adopted, which provides satisfactory results (see section 6.2), consists in requiring that the extrapolated PSFs reproduce the correct flux of the star within the extraction region.

4. The image reconstruction problem

An accurate statistical model of astronomical images detected by a charge-coupled device (CCD) camera is formulated in [56]. In each pixel, the detected image value is essentially the sum of three terms: the number of photo-electrons due to the photons arriving from the astronomical target; the number of photo-electrons due to dark current and sky emission (background); the additive Gaussian noise due to the amplifier through which all pixel values are read, the so-called read-out noise (RON). The first two terms are realizations of independent Poisson random variables, so that the noise is a mixture of Gaussian and Poisson noise. However, in the case of images with a large background, a sufficiently accurate approximation is obtained by adding the variance σ^2 of the RON to the image (thus modifying the background) and approximating the RON as a Poisson process with expected value σ^2 [57], so that the values of an astronomical image, augmented by σ^2 , can be modeled as independent Poisson processes.

In the case of LN images, such a model is applicable to the reference image (i.e. the non-de-rotated one) but is not applicable to the de-rotated images, because numerical de-rotation introduces correlation between different pixels. The Poisson model is applicable if one does not de-rotate the images and introduce the rotation of the object in the imaging model used in the iterative reconstruction algorithms. The disadvantage of this approach is that it is computationally expensive and the application of the rotation matrix at each iteration can introduce severe artifacts. Therefore, we assume that all images are realizations of Poisson processes, even if this approximation is not accurate for the de-rotated ones.

4.1. Maximum likelihood approach

Let p be the number of detected LN images of the same target. As follows from section 2.1, the de-rotated images are immersed into broader arrays, all with the same size, and are surrounded by zeros. The set of the values of the multi-index $\mathbf{n} = \{n_1, n_2\}$ characterizing the pixels of these broader arrays is denoted by \bar{S} and the subset of the values of the same multi-index corresponding to the pixels of the j th de-rotated image by $S_j \subset \bar{S}$; finally, S is the intersection of the sets S_j , and corresponds, in general, to a ‘polygonal’ domain interior to the ‘square’ corresponding to \bar{S} [41]. If the image of the scientific target is contained in a sub-domain of the full image, then one can extract a squared array containing this sub-domain and S can be the set of indices corresponding to this array; this is, of course, the most favorable situation for image reconstruction. In any case, one can extract from each image the part corresponding to S and add the variance σ^2 of the RON to the result. These images are denoted as \mathbf{g}_j ($j = 1, \dots, p$). Similarly the backgrounds \mathbf{b}_j ($j = 1, \dots, p$) are the backgrounds estimated in the preprocessing step, augmented by the constant σ^2 .

Next let \mathbf{f} be the scientific target (called the *object* in the following) which generates the images \mathbf{g}_j . It may be contained in the domain of these images but, in a more general situation, it may be defined in a broader domain, so that, thanks to the blurring, the values of \mathbf{g}_j , in pixels close to the boundary, receive contributions from the values of \mathbf{f} in pixels external to

the image domain. The set of indices corresponding to the object domain is denoted by R and, in general, $S \subset R \subset \bar{S}$.

Finally, let us assume that space-invariant PSFs \mathbf{K}_j ($j = 1, \dots, p$) can be extracted from the different images and extended to R by applying the procedure described in section 2.2. They are usually normalized to the unit flux (ℓ_1 norm) on R :

$$\sum_{\mathbf{n} \in R} \mathbf{K}_j(\mathbf{n}) = 1, \quad j = 1, \dots, p. \quad (2)$$

A further extension to $S + R$ can be obtained by periodic continuation. We stress that these PSFs can be very broad, as a consequence of seeing. For instance, in the case of the PSF of figure 4, 77% of the flux is contained in the region of AO correction, which has a diameter of about 160 pixels; this value reduces to 57% in the case of a PSF with SR of the order of 34%. Therefore, a relevant amount of flux is contained in the outer region due to seeing.

If we introduce the following matrices A_j and A_j^T

$$(A_j \mathbf{f})(\mathbf{m}) = \sum_{\mathbf{n} \in R} \mathbf{K}_j(\mathbf{m} - \mathbf{n}) \mathbf{f}(\mathbf{n}), \quad \mathbf{m} \in S, \quad (3)$$

$$(A_j^T \mathbf{g})(\mathbf{n}) = \sum_{\mathbf{m} \in S} \mathbf{K}_j(\mathbf{m} - \mathbf{n}) \mathbf{g}(\mathbf{m}), \quad \mathbf{n} \in R, \quad (4)$$

and if we assume that all the $\mathbf{g}_j(\mathbf{m})$ ($j = 1, \dots, p$; $\mathbf{m} \in S$) are realizations of independent Poisson processes, with expected values given by $(A_j \mathbf{f} + \mathbf{b}_j)(\mathbf{m})$, then the likelihood is the product of all Poisson distributions of these processes. If one applies the usual procedure of taking the negative logarithm of the likelihood and rearranging terms independent of \mathbf{f} , then the maximization of the likelihood is equivalent to the minimization of the following function on the nonnegative orthant:

$$J_0(\mathbf{f}; \mathbf{g}) = \sum_{j=1}^p \sum_{\mathbf{m} \in S} \left\{ \mathbf{g}_j(\mathbf{m}) \ln \frac{\mathbf{g}_j(\mathbf{m})}{(A_j \mathbf{f} + \mathbf{b}_j)(\mathbf{m})} + (A_j \mathbf{f} + \mathbf{b}_j - \mathbf{g}_j)(\mathbf{m}) \right\}, \quad (5)$$

where \mathbf{g} is the set of the p detected images \mathbf{g}_j and \mathbf{f} is the unknown object. We call $J_0(\mathbf{f}; \mathbf{g})$ the *data-fidelity function*; it is a sum of generalized Kullback–Leibler (KL) divergences (or Csiszár I-divergence [25]), one for each image. From known properties of these functions, it follows that $J_0(\mathbf{f}; \mathbf{g})$ is *nonnegative*, *convex* and *coercive*, so that absolute minimizers of this function exist, the so-called maximum likelihood (ML) solutions of the image reconstruction problem.

Remark 1. In our application, the function $J_0(\mathbf{f}; \mathbf{g})$ is, in general, strictly convex so that the minimizer is unique. Indeed, the gradient and Hessian are given by

$$\nabla J_0(\mathbf{f}; \mathbf{g}) = \sum_{j=1}^p \left\{ \boldsymbol{\alpha}_j - A_j^T \frac{\mathbf{g}_j}{A_j \mathbf{f} + \mathbf{b}_j} \right\}, \quad (6)$$

$$\nabla^2 J_0(\mathbf{f}; \mathbf{g}) = \sum_{j=1}^p A_j^T \frac{\mathbf{g}_j}{(A_j \mathbf{f} + \mathbf{b}_j)^2} A_j, \quad (7)$$

where the quotient of two arrays is defined in the Hadamard sense, i.e. pixel by pixel, and the $\boldsymbol{\alpha}_j$ are the arrays defined by

$$\boldsymbol{\alpha}_j(\mathbf{n}) = \sum_{\mathbf{m} \in S} \mathbf{K}_j(\mathbf{m} - \mathbf{n}), \quad \mathbf{n} \in R. \quad (8)$$

In the case $R = S$, these arrays are just $\mathbf{1}$, the constant array with all entries equal to 1, thanks to the normalization and periodic extension of the PSFs.

The Hessian is positive definite if and only if at least one image \mathbf{g}_j is strictly positive and the corresponding matrix A_j is nonsingular. In the application to infrared imaging, data are characterized by a large background and also contain the positive constant σ^2 (for the LN detector, $\sigma = 10 e^-/\text{px}$), so that they are strictly positive. As concerns the non-singularity of the matrices A_j , we expect that it also holds true, at least in the case $R = S$, because, even if the imaging system is band-limited, we only have approximate estimates of the PSFs, so that their DFT does not contain zeros. In any case, one can verify if this property holds true.

4.2. Bayesian approach

The minimizers of $J_0(\mathbf{f}; \mathbf{g})$ in general do not provide a reliable solution of the reconstruction problem, except in some specific cases, such as a star cluster (see [13] for a discussion). Such a situation is due to the fact that these minimizers are sparse objects, as proved in [9], the so-called *night-sky solutions*.

In the case of more complex objects (nebulae, galaxies, etc), reliable solutions can be obtained by means of the Bayesian approach [30, 31, 40], which is an extension of the well-known Tikhonov regularization of ill-posed inverse problems. In the case of priors with an exponential form, such as the Gibbs priors, the computation of the *maximum a posteriori* (MAP) estimate is equivalent to the minimization of a function with the following structure [40, 13]:

$$J(\mathbf{f}; \mathbf{g}) = J_0(\mathbf{f}; \mathbf{g}) + \mu J_1(\mathbf{f}), \quad \mathbf{f} \geq 0, \quad (9)$$

where $\mu J_1(\mathbf{f})$ is the negative logarithm of the prior, modulus terms independent of \mathbf{f} . We call $\mu > 0$ the *regularization parameter* and $J_1(\mathbf{f})$ the *regularization function*. If the data-fidelity function $J_0(\mathbf{f}; \mathbf{g})$ is strictly convex, then the MAP estimate is unique for each value of μ .

In our work, we have investigated a number of convex and non-convex regularization and, in particular, the following ones.

- Tikhonov regularization function

$$J_1(\mathbf{f}) = \frac{1}{2} \|(I - D)\mathbf{f}\|^2, \quad (10)$$

where $\|\cdot\|$ denotes the usual ℓ_2 norm and D is a matrix with nonnegative entries. If $D = 0$, then we have the standard Tikhonov regularizer while if D is obtained from the 3×3 mask with zero values in the center and the four corners and 1/4 in the other positions, then we have regularization in terms of the ℓ_2 norm of the discrete Laplacian.

- Edge-preserving regularization function [22]

$$J_1(\mathbf{f}) = \frac{1}{2} \sum_{\mathbf{n} \in R} \sum_{\mathbf{n}' \in \mathcal{N}(\mathbf{n})} \psi \left[\left(\frac{\mathbf{f}(\mathbf{n}) - \mathbf{f}(\mathbf{n}')}{\delta_{\mathbf{n}, \mathbf{n}'}} \right)^2 \right], \quad (11)$$

where $\mathcal{N}(\mathbf{n})$ is a symmetric neighborhood of \mathbf{n} containing only horizontal and vertical first neighbors or horizontal, vertical and diagonal first neighbors; in such a case $\delta_{\mathbf{n}, \mathbf{n}'} = 1$ for horizontal/vertical neighbors, and $\delta_{\mathbf{n}, \mathbf{n}'} = \sqrt{2}$ for diagonal neighbors. Moreover,

$$\psi(t) = \sqrt{t + \eta^2}, \quad (12)$$

with η a thresholding parameter.

- High-dynamic range regularization function [5]

$$J_1(\mathbf{f}) = \frac{\eta^2}{2} \sum_{\mathbf{n} \in R} \frac{|\mathbf{f}(\mathbf{n})|^2}{|\mathbf{f}(\mathbf{n})|^2 + \eta^2}, \quad (13)$$

where η is also a thresholding parameter; in the regions where \mathbf{f} is large with respect to η , for instance a bright star, we have no regularization, while in the regions where \mathbf{f} is small with respect to η , for instance a faint and diffuse object, we have a Tikhonov-like regularization.

In our simulations, we also considered entropy regularization but without success, presumably because entropy is enforcing sparsity [28], and the minimizers of $J_0(\mathbf{f}; \mathbf{g})$ are already sparse. For this reason, we also do not consider regularization in terms of the ℓ_1 norm in pixel space.

4.3. Selection of the regularization parameter

One of the major problems in the Bayesian approach is the selection of a suitable value of the regularization parameter. To our knowledge, in the case of regularization of the KL divergence, only a few have been proposed [8, 14]. That proposed in [14] can be easily applied to our problem. It is based on the remark that if in equation (5) \mathbf{f} is replaced by the true object $\bar{\mathbf{f}}$ and if the expected number of photons is large (a condition always satisfied in the case of LN imaging), then the expected value of a single term in the sum is approximately $1/2$. Therefore, the terms of $J_0(\bar{\mathbf{f}}; \mathbf{g})$ fluctuate around $1/2$ and positive fluctuations may compensate the negative ones. In conclusion, we expect that the value of the data fidelity function, with $\mathbf{f} = \bar{\mathbf{f}}$, is approximately $\#(S)p/2$, where $\#(S)$ is the cardinality of S .

Let \mathbf{f}_μ^* be the (unique) minimizer of (9), and let us introduce the following *discrepancy function*:

$$D_{\mathbf{g}}(\mu) = \frac{2}{\#(S)p} J_0(\mathbf{f}_\mu^*; \mathbf{g}). \quad (14)$$

If, for some value of μ , \mathbf{f}_μ^* is close to the true object, then $D_{\mathbf{g}}(\mu)$ must be close to 1. The following selection rule follows: search for the value of μ such that

$$D_{\mathbf{g}}(\mu) = 1. \quad (15)$$

Since, as proved in [14], $D_{\mathbf{g}}(\mu)$ is an increasing function of μ , the solution of this equation, if it exists, is unique. We call this criterion a *discrepancy principle* for Poisson data. Thanks to the monotonicity of $D_{\mathbf{g}}(\mu)$, the solution of the discrepancy equation can be found in a few steps by means of some secant-like method.

It is important however to remark that the previous result is correct if the exact PSFs are known. If we have only approximate PSFs $\mathbf{K}_j^{(a)}$ and if we denote as $J_0^{(a)}(\mathbf{f}; \mathbf{g})$ the corresponding data fidelity function, then it is not difficult to prove that the value of this function computed at $\mathbf{f} = \bar{\mathbf{f}}$ is certainly greater than 1 (the value depends on the approximation of the PSFs as well as on the object), but it is close to 1 for background-dominated images (see section 6.2).

5. Algorithms

Before analyzing algorithms for the solution of the minimization problems introduced in the previous section, we briefly discuss a very simple approach to the reconstruction of LN images [37]. The idea is to co-add the p images in a single one, $\mathbf{g}^{(p)} = \mathbf{g}_1 + \dots + \mathbf{g}_p$, which is also a realization of a Poisson process with the expected value $\mathbf{K}^{(p)} * \mathbf{f}^{(p)} + \mathbf{b}^{(p)}$, where

$$\mathbf{K}^{(p)} = \frac{1}{p} \sum_{j=1}^p \mathbf{K}_j, \quad \mathbf{f}^{(p)} = p\mathbf{f}, \quad \mathbf{b}^{(p)} = \sum_{j=1}^p \mathbf{b}_j. \quad (16)$$

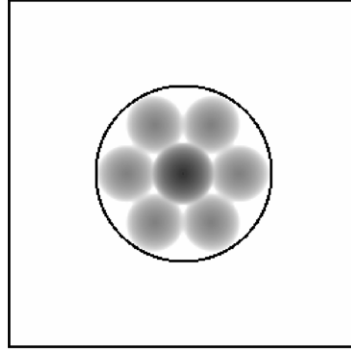


Figure 5. Plot of the superposition of the MTSs of three equispaced images, showing the coverage, in the Fourier plane, of the band of a 22.8 m telescope, indicated by the circle. The MTSs are small but not zero in the white domain around the central disk corresponding to the band of a 8.4 m telescope.

After co-adding one can apply, for instance, the standard algorithm for the reconstruction of astronomical images, the so-called Richardson–Lucy (RL) algorithm [52, 47] (also called EM in emission tomography [54])

$$\mathbf{f}^{(k+1,p)} = \mathbf{f}^{(k,p)} [A^{(p)}]^T \frac{\mathbf{g}^{(p)}}{A^{(p)}\mathbf{f}^{(k,p)} + \mathbf{b}^{(p)}}, \quad (17)$$

where $A^{(p)}$ is the circulant matrix associated with the PSF $\mathbf{K}^{(p)}$.

However, if one looks at the effect of co-adding in Fourier plane by taking into account the structure of the band of the instrument as shown in figure 4 (upper-right panel), one finds that it increases the signal-to-noise ratio (SNR) in the central disk (corresponding to the 8.4 m telescope) while it decreases the SNR in the side disks that are due to interferometry and contain the relevant information required for improving resolution. Indeed, since a rotation of the image corresponds to a rotation of the band, the co-adding is equivalent to adding the out-of-band noise of one image to the interferometric signal of another one, as one can easily understand by looking at the subsequent figure 5. In the next section, we will give a demonstration of the possible negative effects of this approach.

5.1. Iterative algorithms for the ML approach and stopping rules

In the case of minimization of the function $J_0(\mathbf{f}; \mathbf{g})$, the most natural approach is to apply the EM method in the form considered by Shepp and Vardi [54]. The result is the following iterative algorithm, denoted in the following as *multiple image RL*:

- initialize with $\mathbf{f}^{(0)} > 0$ (in general, a constant array);
- for $k = 0, 1, 2, \dots$, given $\mathbf{f}^{(k)}$, compute

$$\mathbf{f}^{(k+1)} = \frac{\mathbf{f}^{(k)}}{\alpha} \sum_{j=1}^P A_j^T \frac{\mathbf{g}_j}{A_j \mathbf{f}^{(k)} + \mathbf{b}_j}. \quad (18)$$

Here α is the sum of the arrays α_j defined in equation (8):

$$\alpha(\mathbf{n}) = \sum_{j=1}^P \alpha_j(\mathbf{n}), \quad \mathbf{n} \in R. \quad (19)$$

Since the previous algorithm is basically the EM algorithm of Shepp and Vardi, the several convergence proofs proposed for this algorithm (see, for instance, [48]) can also be applied to the present one. However, it is important to remark that these convergence proofs hold true in the case of zero background (they require the condition of flux conservation implicit in the standard EM algorithm), while, in the case of infrared observations, the images are characterized by very large backgrounds. Therefore, a complete proof of the convergence of the previous algorithm is not available, at least as far as we know. But this lack of proof is not very relevant. The important remark is that the previous algorithm is a scaled gradient method. Indeed, using the expression (6) of the gradient, it is easy to verify that the iteration (18) can be written in the following form:

$$\mathbf{f}^{(k+1)} = \mathbf{f}^{(k)} - \frac{\mathbf{f}^{(k)}}{\alpha} \nabla J_0(\mathbf{f}^{(k)}; \mathbf{g}), \quad (20)$$

and acceleration and convergence can be obtained, for instance, by means of a line search method or by means of the general algorithm named the *scaled gradient projection* (SGP) method [17]. Work is in progress in this direction.

In a first attempt of accelerating the previous algorithm, which is terribly slow, one can apply the technique of *ordered subsets*, proposed for emission tomography [38] and successfully used in practice. Indeed, one LN image is characterized by a well-defined direction as a projection in 2D tomography. Therefore, the application of OSEM to the reconstruction of LN images is straightforward and leads to the following iterative algorithm [10]:

- initialize with $\mathbf{f}^{(0)} > 0$;
- for $k = 0, 1, 2, \dots$, given $\mathbf{f}^{(k)}$, set $\mathbf{h}^{(0)} = \mathbf{f}^{(k)}$ and, for $j = 1, \dots, p$, compute

$$\mathbf{h}^{(j)} = \frac{\mathbf{h}^{(j-1)}}{\alpha_j} \left(A_j^T \frac{\mathbf{g}_j}{A_j \mathbf{h}^{(j-1)} + \mathbf{b}_j} \right); \quad (21)$$

- set $\mathbf{f}^{(k+1)} = \mathbf{h}^{(p)}$,

each iteration being a cycle over the detected images.

Remark 2. It is important to point out the main differences between LN imaging and tomography. While in tomography the number of projections is large, the number of LN images will be necessarily small; presumably a reasonable number will be 3 and this small number can be sufficient for obtaining satisfactory reconstruction. In figure 5, we show the domain in the Fourier plane where information is provided by a set of three equispaced images (angles 0° , 60° and 120°) and we see that it corresponds to an almost complete coverage of the circular band of a 22.8 m telescope, indicated by the circle. Therefore, a deconvolution of these three images can provide the required resolution.

Another important difference is that, in LN imaging, the different images can have very different fluxes, i.e. ℓ_1 norms, because they are acquired with different integration times (the available integration time may depend on the position of the target in the sky). Variations of the ℓ_1 norm of the images inside the OSEM cycle generate oscillations of the $\mathbf{h}^{(j)}$, an effect which must be avoided. For this reason, it is important to renormalize the images in such a way that they have all the same ℓ_1 norm. The arithmetic mean of the fluxes of the detected images can be a solution.

The previous remark implies that the improvement of efficiency provided by OSEM in our application is not very large. In numerical simulations, we verified that, with p images, OSEM provides a reduction in the number of iterations by a factor p , as expected. However, the computational cost of one OSEM iteration is slightly greater than that of one multiple image RL iteration. The latter requires $3p + 1$ FFTs while one OSEM iteration requires $4p$ FFTs.

Therefore, in the case of three images, the reduction in computation time provided by OSEM is a factor of about 2.5; not very large but not negligible since, in several cases, thousands of iterations are required.

In the case of squared arrays and normalized and periodic PSFs, the normalization of the PSFs implies that the sets of indices corresponding to the p images (the subsets of OSEM) are balanced in the sense of [38]. Therefore, we did not attempt to use the block-iterative methods proposed by Byrne [19, 20], even if it should be interesting to check if they can provide an improvement of efficiency. We also remark that the balance of the subsets ensures convergence of the algorithm in the consistent case (i.e. the linear equation has nonnegative solutions), a situation never occurring in practice. In the inconsistent case, convergence to a limit circle of p images is expected. However, these images should be very similar because we always found numerical convergence of the algorithm.

Finally, except in the case of point-wise objects, early stopping of the iterations is required for obtaining sensible solutions, so that stopping rules must be used. We mention two of them. The first is usable only in the case of numerical simulations, since it requires the knowledge of the true object $\bar{\mathbf{f}}$; it consists in stopping the iteration when the relative r.m.s. error, defined by

$$\rho^{(k)} = \frac{\|\mathbf{f}^{(k)} - \bar{\mathbf{f}}\|}{\|\bar{\mathbf{f}}\|}, \quad (22)$$

reaches a minimum value. The second is based on the discrepancy principle described in the previous section and consists in stopping the iteration when the discrepancy function

$$D^{(k)} = \frac{2}{\#(S)p} J_0(\mathbf{f}^{(k)}; \mathbf{g}) \quad (23)$$

crosses 1. This criterion can also be obviously applied in the case of real data and therefore it is important to verify its validity by means of numerical simulations, at least in the case of exact PSFs. On the other hand, we did not check the criterion proposed in [60].

5.2. Algorithms for the Bayesian approach

A very simple method for the minimization of the function (9) is the so-called *one-step-late* (OSL) method of Green [32]; indeed it is based on a simple modification of the EM (or RL) algorithm. It is a scaled gradient method, but the scaling may take negative values if the regularization parameter is not sufficiently small [13]. For this reason, it may be convenient to consider the so-called *split-gradient method* (SGM) [43, 1], which also consists in a simple modification of the RL method and is a scaled gradient method with a positive scaling. When the gradient of the regularization function is nonnegative on the nonnegative orthant, it coincides with the OSL method.

The approach is based on the decomposition of the gradient of the regularization function of the following form:

$$-\nabla J_1(\mathbf{f}) = U_1(\mathbf{f}) - V_1(\mathbf{f}), \quad (24)$$

where U_1, V_1 are suitable arrays taking nonnegative values for nonnegative values of \mathbf{f} . This decomposition is not unique but, as shown in [43], a 'natural' one exists for all differentiable regularization functions used in practice. By taking into account equation (6), the negative gradient of the function $J(\mathbf{f}; \mathbf{g})$ is given by

$$-\nabla J(\mathbf{f}; \mathbf{g}) = \left\{ \sum_{j=1}^p A_j^T \frac{\mathbf{g}_j}{A_j \mathbf{f} + \mathbf{b}_j} + U_1(\mathbf{f}) \right\} - \left\{ \sum_{j=1}^p \alpha_j + \mu V_1(\mathbf{f}) \right\}. \quad (25)$$

Then, from the first Karush–Kuhn–Tucker (KKT) condition, $\mathbf{f}\nabla J(\mathbf{f}; \mathbf{g}) = 0$, one derives a fixed point equation and, by applying the method of successive approximations, one obtains the iterative algorithm

- initialize the algorithm with $\mathbf{f}^{(0)} > 0$;
- for $k = 0, 1, 2, \dots$, given $\mathbf{f}^{(k)}$, compute

$$\mathbf{f}^{(k+1)} = \frac{\mathbf{f}^{(k)}}{\boldsymbol{\alpha} + \mu V_1(\mathbf{f}^{(k)})} \left\{ \sum_{j=1}^p A_j^T \frac{\mathbf{g}_j}{A_j \mathbf{f}^{(k)} + \mathbf{b}_j} + \mu U_1(\mathbf{f}^{(k)}) \right\}. \quad (26)$$

It is obvious that for $\mu = 0$, one re-obtains the multiple image RL algorithm; moreover, for the regularization functions such that $U_1 = 0$, one re-obtains the OSL method applied to our problem. This situation occurs, for instance, in the case of the standard Tikhonov regularization function since $\nabla J_1(\mathbf{f}) = \mathbf{f}$, and therefore the gradient is nonnegative on the nonnegative orthant. No convergence proof is available for this algorithm. However, by remarking that it is a scaled gradient method and writing

$$\mathbf{f}^{(k+1)} = \mathbf{f}^{(k)} - \lambda \frac{\mathbf{f}^{(k)}}{\boldsymbol{\alpha} + \mu V_1(\mathbf{f}^{(k)})} \nabla J(\mathbf{f}^{(k)}; \mathbf{g}) \quad (27)$$

(which becomes (26) if $\lambda = 1$) convergence (and a moderate acceleration) can be obtained by searching for a better $\lambda > 1$, using for instance the Armijo rule [43]. Also in this case, the SGP method could be used.

Finally, a block decomposition of the previous expression of the gradient suggests the following OS version of algorithm:

- initialize the algorithm with $\mathbf{f}^{(0)} > 0$;
- for $k = 0, 1, 2, \dots$, given $\mathbf{f}^{(k)}$, set $\mathbf{h}^{(0)} = \mathbf{f}^{(k)}$ and, for $j = 1, \dots, p$, compute

$$\mathbf{h}^{(j)} = \frac{\mathbf{h}^{(j-1)}}{\boldsymbol{\alpha}_j + \frac{\mu}{p} V_1(\mathbf{h}^{(j-1)})} \left\{ A_j^T \frac{\mathbf{g}_j}{A_j \mathbf{h}^{(j-1)} + \mathbf{b}_j} + \frac{\mu}{p} U_1(\mathbf{h}^{(j-1)}) \right\}; \quad (28)$$

- set $\mathbf{f}^{(k+1)} = \mathbf{h}^{(p)}$.

Again, the algorithm reduces to OSEM in the case $\mu = 0$. No convergence proof has been obtained so far.

As concerns the choice of the regularization parameter, in the case of numerical simulation one can minimize the relative r.m.s. error defined as in equation (22), with $\mathbf{f}^{(k)}$ replaced by \mathbf{f}_μ^* , the limit of the algorithm, or one can apply the discrepancy principle described in section 4.3.

5.3. Boundary effect correction

If the object \mathbf{f} is surrounded by a region of free sky which has an angular size of the order of the width of the PSFs, then one can take $S = R$ and compute the matrices $\{A_j, A_j^T\}$ as cyclic convolutions. All the previous algorithms can be efficiently implemented thanks to FFT. Moreover, the normalization condition (2) implies $\boldsymbol{\alpha}_j(\mathbf{n}) = 1$ for any j .

If the previous condition is not satisfied, then we must deal with boundary effects. Approaches for reducing these effects are based on the apodization of the detected image or on the use of boundary conditions (see, for instance, [49, 53]), an approach which is equivalent to extend the image and the object outside the FoV in a somewhat artificial way. However, starting from the observation that the detected images receive contributions from a domain broader than the FoV, the approach proposed in [12, 4] consists in reconstructing the object in a domain $R \supset S$ containing the object or, at least, the parts of the object external

to the FoV which contribute to the images. Since the AO-corrected PSFs of LN are free of zeros (as one can understand from figure 4, the correction is ‘sitting’, in a certain sense, on the PSF of the seeing, which is extremely over-sampled because of the resolution achievable with LN, and therefore very broad with respect to the sampling distance of the detector), the arrays $\alpha_j(\mathbf{n})$ defined in equation (8) are strictly positive. It follows that all the previous algorithms are well defined and could be used to this purpose.

The difficulty is the computation of the matrices $\{A_j, A_j^T\}$. However, if the domain R is selected in such a way that the Fourier transform of arrays defined over R can be computed by means of FFT, a simple algorithmic trick allowing a fast computation of these matrices consists in extending the detected images to R by zero padding and also in extrapolating to R the extracted PSFs. In this way, the matrices $\{A_j, A_j^T\}$ can be computed by means of FFT and the periodic continuation outside R , implicit in this computation, does not produce annoying effects. We remark that also the arrays $\alpha_j(\mathbf{n})$ can be efficiently computed over R if we remark that they are given by $\alpha_j = A_j^T \chi_S$, where χ_S is the characteristic function of S in R .

In this way, all the previous algorithms can be efficiently implemented for reconstructing the unknown object over R . Finally only the reconstruction of the object over S is taken into account, because the reconstruction outside S is not very reliable due to the limited information contained in the detected image. In this way, it is possible to obtain excellent results, with a moderate increase of the computational cost. An example is shown in section 6.1.4.

5.4. Acceleration of the iterative methods

All the algorithms described in the previous sections require, in general, a very large number of iterations. Therefore, efficiency is an important issue in LN imaging: one must look for techniques able to reduce the number of iterations without increasing significantly the computational cost per iteration.

Since algorithms (18) and (26) are scaled gradient methods, as shown in equations (20) and (27), respectively, one can reduce the number of iterations by a line search along the descent direction. However, as remarked in [42], even if one uses an approximate line search, such as the Armijo rule, the average reduction of the overall computation time is about 20%.

A multiplicative relaxation is proposed in [39]. In the case of algorithm (18), it consists in taking a power ω of the sum and arguments are proposed in [42], showing that this modification can provide a reduction of the number of iterations by a factor ω , without a significant increase of the numerical cost per iteration. In the case of EM with background zero, convergence is proved only for $\omega < 2$ [39]. The technique was applied in [2] to the case of LN-imaging and the results of numerical experiments are consistent with the expected reduction of the number of iterations. However, the lack of a proof of convergence when the multiplicative relaxation is applied to OSEM, makes the use of this technique questionable.

Similar criticism can be applied to the acceleration methods proposed in [15, 16], even if these methods are attractive because they can be applied to any iterative method characterized by a slow convergence which has the form $\mathbf{f}^{(k+1)} = T(\mathbf{f}^{(k)})$, with a linear or nonlinear operator T independent of k . These methods are implemented in AIRY and can provide a reduction of the number of iterations by factors of 10 and even more. However, in some critical cases, they do not provide the correct result. One example is provided by the reconstruction of the binary discussed at the beginning of the next section.

Work is in progress for exploring the gain provided by the application of SGP [17] to the various scaled gradient methods introduced in the previous sections. As already remarked, this method is sound because its convergence is proved. However, it is not applicable to the OS versions of the previous algorithms.

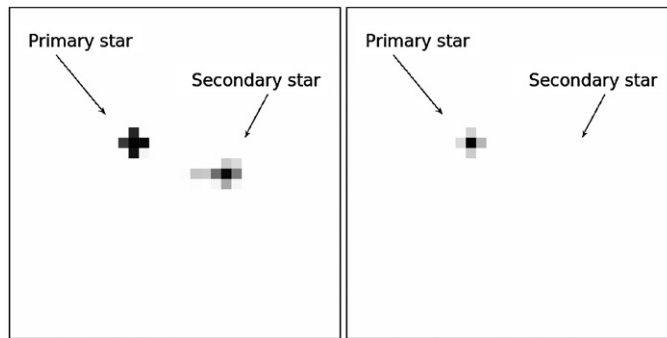


Figure 6. Reconstruction of the binary with $\Delta m = 10$ (log scale). Left panel: OSEM reconstruction. Right panel: co-adding approach reconstruction; the faint star is lost.

6. Simulation analysis

Numerical experiments demonstrate that OSEM is superior to the co-adding approach both in accuracy and efficiency [2]. However, to emphasize the need of multiple image algorithms, we first discuss a critical case where the co-adding approach does not provide the correct result. The object is a binary observed in the K-band ($\lambda = 2.2 \mu\text{m}$): the magnitude of the primary is $m_1 = 10$ and that of the secondary $m_2 = 20$. The distance between the two stars is 45 mas and the axis of the binary forms an angle of 23° with the direction of the baseline of the first image. Moreover, three images at 0° , 60° and 120° are generated using PSFs with $\text{SR} = 70\%$ and a constant background of $13.5 \text{ mag arcsec}^{-2}$ is added to them. Finally, by assuming an integration time of 10 min per image, they are perturbed with Poisson noise and additive Gaussian noise with $\sigma = 10 e^-/\text{px}$, a reasonable figure for the LN detector. The average number of photons/pixel emitted by the background is about 3.2×10^3 , that of the primary 3.2×10^9 and that of the secondary 3.2×10^5 .

We perform 20 000 iterations of OSEM, applied to the three images, and of RL, applied to the single co-added image. The magnitudes of the two stars are computed at each iteration by computing the flux on 3×3 squares centered on their known positions. Both methods start with a magnitude of the secondary of about 35, but while the magnitude provided by RL increases indefinitely, that provided by OSEM starts to decrease after 1000 iterations for reaching a value of about 20 after 10 000 iterations. Figure 6 shows the final results: the co-adding approach is unable to detect the faint secondary. Therefore, multiple image methods are preferable because they are more accurate and also more efficient.

6.1. Reconstructions with exact PSFs

In this section, we discuss a few examples of numerical experiments where one assumes that the PSFs are exactly known. This situation never occurs in practice, but these experiments demonstrate the best results achievable for a given set of images, by means of the reconstruction method one is investigating. In all cases, we assume observations in the K band (hence with the background magnitude used in the previous example), three equispaced images and PSFs with $\text{SR} = 70\%$ (except in the case of the planetary surface). The effects of incomplete coverage of the Fourier plane and PSF smearing are discussed in [21].

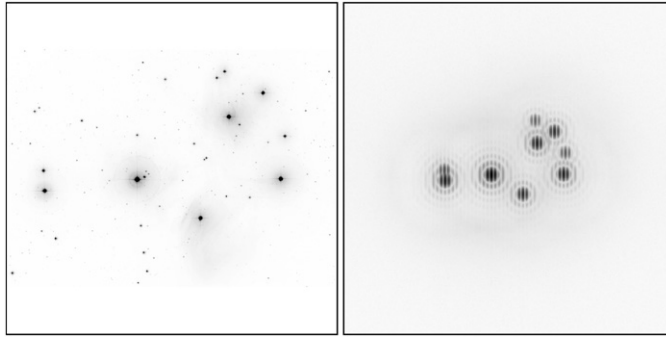


Figure 7. Model of the open cluster. Left: an image of the Pleiades showing the nine brightest images. Right: one of the three interferometric images of the model of the open star cluster obtained by rescaling the Pleiades image.

6.1.1. Open star cluster. The model of an open star cluster is derived from a rescaled image of the Pleiades, shown in the left panel of figure 7. It consists of nine stars with magnitudes ranging from 12.86 to 15.64 and an interferometric image of it is shown in the right panel. Since the stars are sufficiently bright, we assume an integration time of 2 min per image. In this case, as expected, OSEM provides a very good reconstruction and regularization is not required since we are considering a sparse object. The magnitudes of the stars reach the correct value after about 1000 iterations. If we define a mean absolute error (MAE) as ($q = 9$, in our case)

$$\text{MAE} = \frac{1}{q} \sum_{j=1}^q |m_j - \bar{m}_j|, \quad (29)$$

where the m_j are the magnitudes of the reconstructed stars and \bar{m}_j the original ones, then we find a MAE of the order of 2×10^{-4} . If we increase the integration time, so that the noise decreases, then the number of iterations to convergence increases and the MAE decreases but it is obvious that the previous result is sufficiently accurate.

6.1.2. Super-resolution. It is known that RL has a moderate super-resolution effect. As a consequence, OSEM is able to resolve a pair of stars with an angular distance smaller than the resolution distance of LN, 20 mas (four pixels) in the K band. However, it is possible to increase this effect by a suitable initialization of OSEM. Indeed, if the object is contained in a domain with an angular size not much greater than the angular resolution of the instrument, a further improvement of resolution is achievable by restricting the reconstruction to this domain. This restriction can be obtained by initializing OSEM with the mask of the domain: if the initial guess is zero in one pixel, then all iterations will be zero in that pixel. A considerable improvement of resolution can be obtained in this way. However, it should require an oversampling of the data much greater than that provided by the LN detector. A discussion of the method as well as of a possible oversampling by means of data re-binning is discussed in [3].

6.1.3. Diffuse objects. The model of diffuse object is an image of the planetary nebula (actually a dying star) NGC7027, pushed at a distance such that its angular size is of the order of $2''$. We consider three versions with three different integrated magnitudes: 10, 15 and 18. If we assume the same integration time (20 min in our experiment) in the three cases, then the

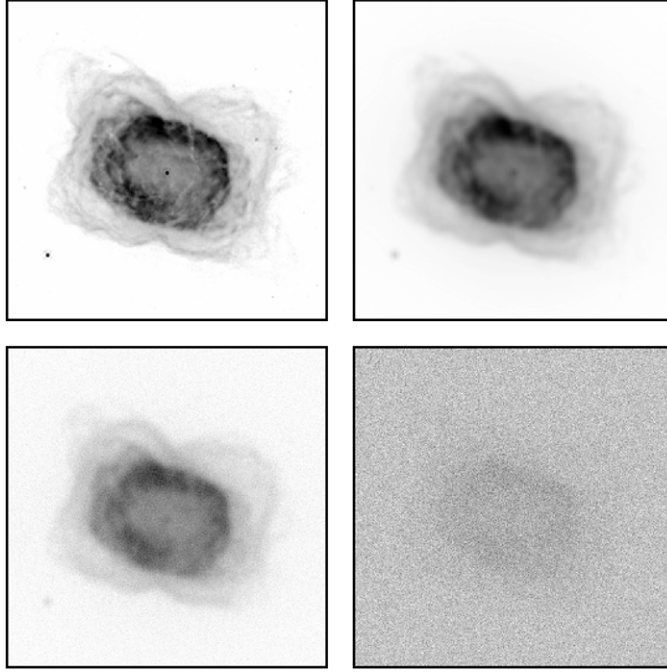


Figure 8. Infrared image of the planetary nebula NGC7027 (upper-left panel) and three LN images (with vertical fringes), respectively, in the case of magnitude 10 (upper-right panel), 15 (lower-left) and 18 (lower-right). Integration time of 20 min.

noise increases with increasing magnitude. In figure 8, we show the nebula and the three LN images (with vertical fringes) corresponding to the three magnitudes.

By stopping OSEM at the minimum relative r.m.s. error, as defined in equation (22), one finds, in the three cases, errors of about 3%, 9% and 31%; as expected, the error increases with increasing magnitude. These values are very close to the values provided by the discrepancy principle. The two acceleration methods of Biggs and Andrews provide essentially the same results, with a reduction of the number of iterations ranging from 5 to 10.

In this case, regularization of the KL divergence can provide an improvement of the reconstructions achievable with an early stopping of OSEM. Two kinds of regularization functions are considered: the first is the ℓ_2 norm of the discrete Laplacian (10); the second the edge-preserving function of equation (11) (with $\eta = 1$ in equation (12)). We give the functions U_1, V_1 used in the iterative algorithms we implemented. For the Laplacian, they are given by

$$U_1(\mathbf{f}) = (D + D^T)\mathbf{f}, \quad V_1(\mathbf{f}) = (I + D^T D)\mathbf{f}, \quad (30)$$

while for edge-preserving they are given by

$$[U_1(\mathbf{f})](\mathbf{n}) = \sum_{\mathbf{n}' \in \mathcal{N}(\mathbf{n})} \psi' \left[\left(\frac{\mathbf{f}(\mathbf{n}) - \mathbf{f}(\mathbf{n}')}{\delta_{\mathbf{n}, \mathbf{n}'}} \right)^2 \right] \frac{\mathbf{f}(\mathbf{n}')}{\delta_{\mathbf{n}, \mathbf{n}'}} \quad (31)$$

$$[V_1(\mathbf{f})](\mathbf{n}) = \sum_{\mathbf{n}' \in \mathcal{N}(\mathbf{n})} \psi' \left[\left(\frac{\mathbf{f}(\mathbf{n}) - \mathbf{f}(\mathbf{n}')}{\delta_{\mathbf{n}, \mathbf{n}'}} \right)^2 \right] \frac{\mathbf{f}(\mathbf{n})}{\delta_{\mathbf{n}, \mathbf{n}'}} \quad (32)$$

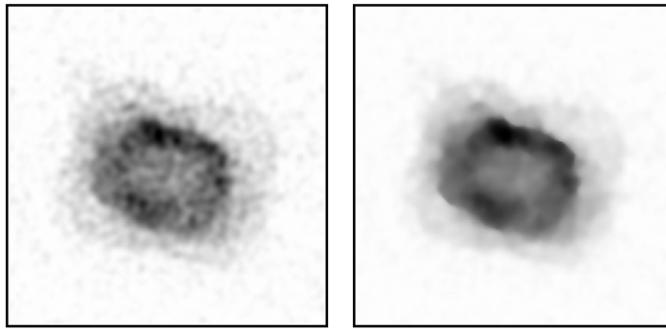


Figure 9. Regularized reconstructions of the image of NGC7027 in the case $m = 18$: Laplacian regularization (left panel) and edge-preserving regularization (right panel).

The values of the regularization parameters obtained by minimizing the relative r.m.s. error or applying the discrepancy principle are very close and therefore provide very similar results. While in the case $m = 10$ regularization does not improve significantly OSEM reconstruction (the error is always of the order of 3% and also visual inspection does not detect significant differences), in the two other cases the improvements are significant. If $m = 15$, then the Laplacian regularization reduces the error from 9% to 7% and edge-preserving regularization from 9% to 8%; if $m = 18$, Laplacian regularization reduces the error from 31% to 16% and edge-preserving from 31% to 15%. Therefore, in the case of faint diffuse objects, regularization seems to be very important even if the reconstructions provided by the two methods are quite different, as shown in figure 9; cartoon effects are evident in the edge-preserving reconstruction.

6.1.4. Boundary effects correction. We recall that boundary effects appear in image deconvolution if the object contained in the FoV is not surrounded by free sky. Indeed, due to the extent of the PSFs, the values of an image in the pixels close to the boundary receive contributions from values of the object outside the FoV. In section 5.3, we briefly discussed a simple way for implementing the idea of removing boundary effects in the iterative algorithms by reconstructing the object in a suitable domain broader than the FoV. It is obvious that this idea is applicable to non-regularized as well as regularized algorithms. Here we demonstrate the accuracy of the approach by a simple example.

The object is again the nebula NGC7027 with $m = 15$. In the left panel of figure 10, we show the reconstruction obtained with OSEM (for simplicity we do not consider regularized algorithms). In the experiment, the 512×512 images are split into four 256×256 parts which are immersed, by zero padding, in 512×512 arrays and are deconvolved, using the same PSFs, by means of the version of OSEM where the α_j are given by equation (8). The four quadrants are extracted from the four reconstructions and recombined (mosaic) to provide a reconstruction of the complete object. The result is shown in the right panel of figure 10. Some residual boundary effects are still visible but they can easily be removed by considering slightly superimposed sub-domains.

This approach is very promising for the deconvolution of very large images using parallel processors or for application to the case of space-variant PSFs. We also remark that if the object is contained in a sub-domain of the full LN images and this domain is extracted for subsequent deconvolution, the application of this technique for boundary effects correction can

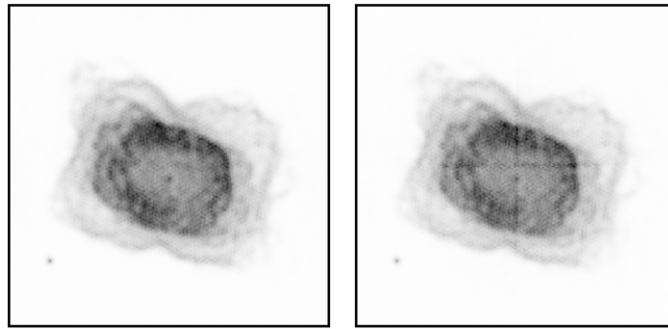


Figure 10. Example of boundary effect correction. Left: reconstruction of the full image (NGC7027 with $m = 15$). Right: mosaic formed by the reconstructions of the four quadrants; the cross visible in the center is a residual boundary effect.

be recommended because the extracted image can contain small contribution from surrounding objects.

6.1.5. Planetary surfaces. The example of the planetary nebula demonstrates that edge-preserving regularization can be useful in the case of faint diffuse objects. However, examples of astronomical objects with sharp edges can be found in the imaging of planetary surfaces. We mention that an image of Jupiter's moon Io was used in the very first simulations intended to demonstrate the efficacy of Fizeau interferometry with LBT (<http://www.lbto.org/why.htm>).

In the same vein from a raw infrared LBT image of Io provided by Carmelo Arcidiacono, after deconvolution, we generated a piecewise constant model of the surface of the planet. This is shown in the upper-left panel of figure 11. We assume an angular size of 1.15 arcsec (corresponding to 230 pixels) and an integrated magnitude $m = 5$ in the K band, which are reasonable figures. The object is convolved with PSFs with $SR = 10\%$, the usual background in the K band is added to the result and, assuming an integration time of 1 s, the three equispaced images are perturbed with Poisson and Gaussian noise. One of the three images is shown in the upper-right panel of figure 11.

In the lower-left panel, we show the OSEM reconstruction, obtained with 749 OSEM iterations; the minimum reconstruction error is 8.6% and the corresponding value of the discrepancy is 0.9996. The value 1 of the discrepancy is crossed at iteration 698 with no change in the reconstruction error. Some granularity is visible in the flat regions.

As expected, an improvement is obtained by means of the edge-preserving approach (we still use $\eta = 1$ in equation (12)). The minimum error criterion and the discrepancy criterion provide the same value of the regularization parameter, $\mu = 2.01 \times 10^{-4}$; convergence is reached after 1785 iterations and the reconstruction error is 6.55%, considerably smaller than that provided by OSEM. The result is shown in the lower-right panel of figure 11. The granularity in the flat regions is completely removed.

6.1.6. Objects with a high dynamic range. In the case of an image containing both diffuse and point-wise objects, it is known that RL-like methods have different convergence rates for the different objects. We tried to overcome this difficulty by a kind of *adaptive regularization*, acting in different ways on different objects. Our method, however, requires a large difference of brightness between the two kinds of objects (high dynamic range) and an angular separation between them. The reconstruction of a bright star over a diffuse cloud, a case arising in the

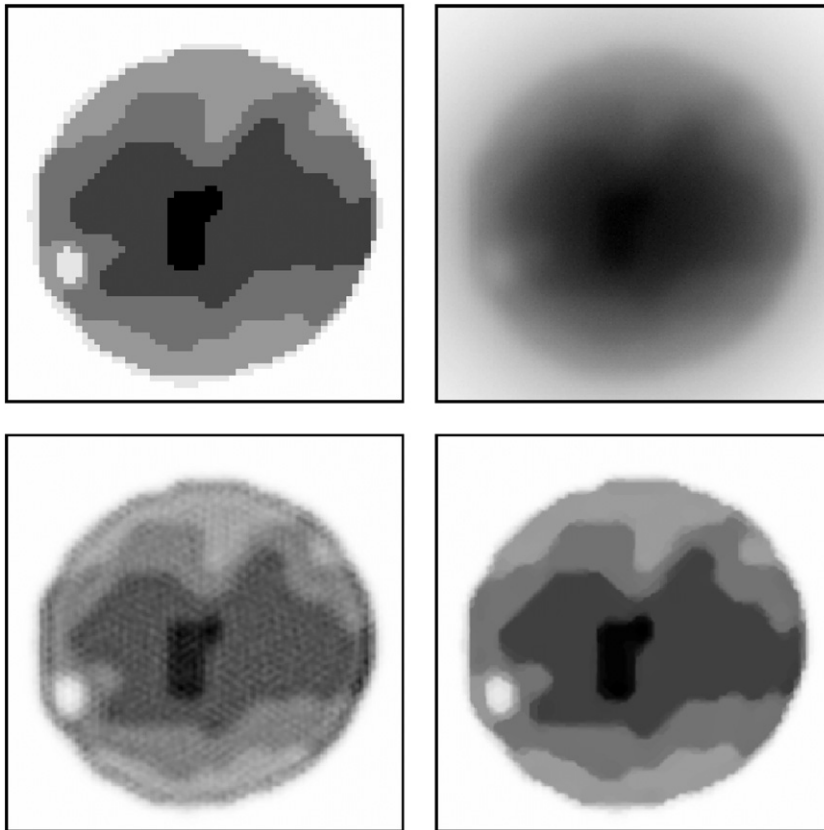


Figure 11. Upper-left: the model of Io surface. Upper-right: the LN image with vertical fringes. Lower-left: OSEM reconstruction. Lower-right: edge-preserving reconstruction.

investigation of young star objects (YSO), cannot be provided by this approach and is an important open problem.

The regularization function proposed in [5] is given in equation (13) and the corresponding functions U_1, V_1 used in the iterative algorithm are given by

$$U_1(\mathbf{f}) = 0, \quad V_1(\mathbf{f}) = \frac{\eta^4 \mathbf{f}}{(\mathbf{f}^2 + \eta^2)^2}. \quad (33)$$

The parameter η is a *thresholding* parameter, ensuring that the reconstruction of the point objects with brightness above η is not regularized, while the reconstruction of the faint objects with brightness below η is regularized in a Tikhonov-like manner. The object with a high dynamic range, used for testing the method, is described in [21, 5]. It is a model of a young binary star, surrounded by a dusty circumbinary ring, inspired by near-infrared observations of the T-Tauri binary star of the quadruple system GG Tauri. It is shown in the upper-left panel of figure 12 and has an extension of about 1.3 arcsec; the integrated magnitude of the ring is 15.25 while the magnitudes of the two stars are 10 and 11, respectively, so that there is about a factor 10^6 between the flux of the primary and the average flux of the ring. The structure of the ring, in terms of level curves, is shown in the upper-right panel of the same figure, while the lower-left and lower-right panels show the best reconstructions of these level curves provided, respectively, by OSEM and the proposed method in the case of PSFs with $SR = 70\%$ and an

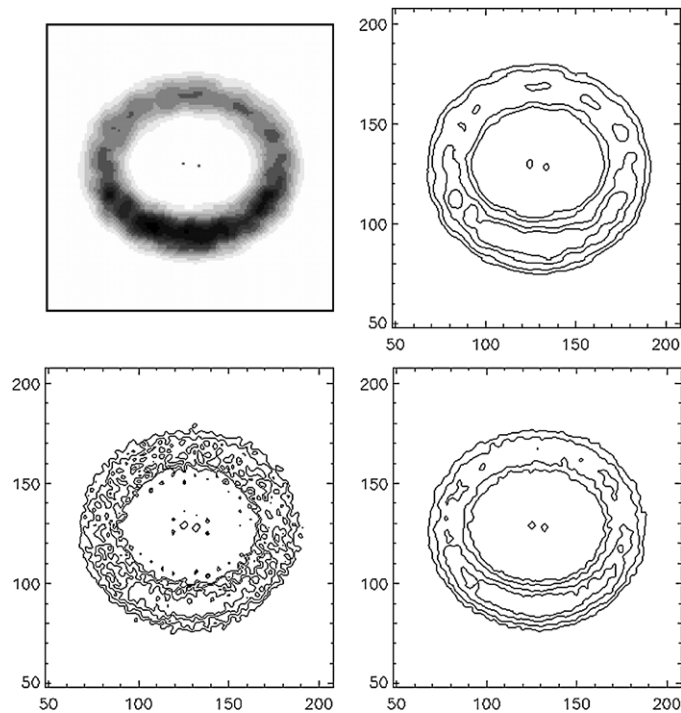


Figure 12. Upper-left: reverse gray level representation of the model of a young binary star described in the text. Upper-right: level curve representation of the ring (values 2460, 4320, 7020, 9720). Lower-left: reconstruction of the same level curves as provided by OSEM. Lower-right: reconstruction of the level curves as provided by the regularization method.

integration time of 20 min. For a discussion of parameter selection, the effect of AO correction and the effect of approximate knowledge of the PSFs, we refer to [5].

6.2. Reconstruction with extracted PSFs

In this section, we briefly discuss a simulation attempting to be closer to reality than the previous ones. It is based on 2048×2048 images containing an astronomical target located in the center of the array and of a star, which can be used for PSF extraction, in the upper-right region. The target is a 256×256 version of NGC7027 (hence with an angular size of about 1 arcsec). We consider again three different integrated magnitudes of the nebula (10, 15 and 18) and three different magnitudes of the star (14, 16 and 18); thus, we have nine different objects. They are convolved with PSFs with $SR = 34\%$ and the results are perturbed with the Poisson and Gaussian noise. One of these images is shown in figure 13 where in the lower-right corner we show the original version of NGC7027. We use a low SR in this simulation because in many instances, the SR of the LN-PSFs will not be so high as one should expect from the performance of the FLAO system of LBT. For simplicity, deconvolution is based on the OSEM algorithm.

In the first instance, images are deconvolved with exact PSFs and iterations are stopped at the minimum r.m.s. error. This procedure provides the best achievable results (at least in the sense of r.m.s. error). Next a circular patch with a diameter of 100 pixels, centered

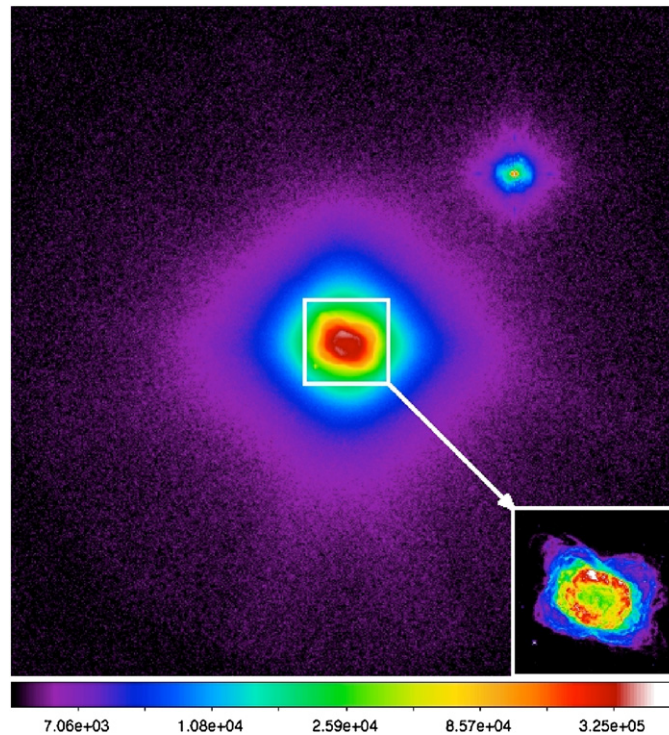


Figure 13. The 2048×2048 image described in the text.

Table 1. Comparison of the results obtained with exact and extracted PSFs. The reconstruction method is OSEM, stopped at the minimum reconstruction error. In the first column the integrated magnitudes of the object; in the second and third column the relative reconstruction errors obtained by deconvolving with the exact and extracted PSFs, respectively; in the fourth and fifth column the corresponding number of iterations (in the case $m = 10$ the minimum is not reached but the error curve is very flat); in the sixth and seventh column the corresponding values of the discrepancy function.

m	Error (%)		Iterations		Discrepancy	
	Exact	Extracted	Exact	Extracted	Exact	Extracted
10	5.56	6.53	>5000	>5000	0.9982	4.9342
15	10.87	11.20	370	310	1.0065	1.0859
18	19.03	18.96	260	260	1.0118	1.0867

on the centroid of the star image, is extracted; the background is estimated and subtracted and the result is extrapolated with a suitable Moffat function, along the lines outlined in section 3.2. The PSFs obtained in such a way are used for a second deconvolution of the images. The results for the three magnitudes of the nebula when the PSFs are obtained from a star with magnitude 14 are reported in table 1. They imply that if the star is sufficiently bright, then the procedure for PSF's extraction and extrapolation provides satisfactory estimates. In the case of the nebula with magnitude 18, the r.m.s. reconstruction error is even smaller in the case of extracted PSFs, but this is certainly due to the particular noise realization. For more significant results, one should consider different realizations of noise and repeat the previous

experiment for each of them. Since the deconvolution of three 2048×2048 images requires hours of computations on our computer, this analysis will be performed when more efficient methods or more efficient processors (or both) will be available.

We comment on the last two columns of table 1. They give the values of the discrepancy function $D^{(k)}$ defined in equation (23) and computed at the iteration number k corresponding to the minimum error. In the case of exact PSFs, the values are very close to 1, thus showing that the stopping criterion based on this discrepancy function works well. The situation is different in the case of extracted PSFs. For the nebula with magnitude 10, the value is about 5 and therefore the stopping criterion based on the discrepancy principle does not work. Clearly, the discrepancy function is strongly dependent on the errors (even reasonably small errors) on the PSFs for this particular object. The situation is changing for the other two magnitudes. The main difference between these two objects and the previous one is that they are fainter so that their images are background dominated. As we have already mentioned, we have preliminary results showing that in the case of background-dominated images, the discrepancy principle can also be used in the case of incorrectly known PSFs. Unfortunately, in the case of background-dominated images, hence of faint objects, the reconstruction error is much larger than in the case of brighter objects.

Results similar to those reported in table 1 are obtained when the PSFs are obtained from stars with magnitudes 16 and 18. In all cases, the β in the Moffat function (1) is optimized by requiring that the PSFs extracted and extrapolated reproduce the flux of the star on the extraction domain. With these PSFs, in the case of the nebula with magnitude 15, the reconstruction error ranges between 11% and 12% and therefore is comparable with the reconstruction error provided by the exact PSFs. If we increase the magnitude of the star, the situation gets worse. For instance, for magnitude 20, the reconstruction error is about 29%. In such a case, a denoising of the extracted image of the star, before extrapolation and β optimization, allows a considerable improvement.

The denoising method used is based on the Bayesian least-squares Gaussian scale mixture (BLS-GSM) approach proposed in [50]. It is a wavelet-based denoising method. The basic assumption is that the wavelet coefficient distribution can be modeled as a Gaussian scale mixture (GSM), which is the product of a Gaussian random vector and an independent hidden random scalar multiplier. From this prior assumption, a Bayesian least-squares estimate of the clean coefficients is derived. The GSM distribution allows us to model the highly kurtotic behavior of the distribution of the wavelet coefficients and also account for a better fit of the tails than the Gaussian or Laplacian distribution. In the framework of BLS-GSM, the full steerable pyramid (FSP) transform is used. The FSP is an over-complete tight frame, to decompose the image in a set of wavelet coefficients, is characterized by shift and rotation invariance and can be adapted to any number of scales and orientations [55].

BLS-GSM is designed to work with white Gaussian noise; thus, one needs to modify the algorithm to deal with the problem at hand (Poisson noise). One can add a simple yet effective preprocessing step: introduce a variance-stabilizing transform, such as the Anscombe transform [6], to approximately convert the Poisson noise to Gaussian noise with unit variance:

$$\tilde{g} = 2\sqrt{g + \frac{3}{8}}. \quad (34)$$

The obtained image \tilde{g} is filtered with BLS-GSM and, at the end of the filtering process, the inverse Anscombe transform is applied.

If this denoising method is applied to the extracted images of a star with $m = 20$, the corresponding PSFs obtained with the extrapolation procedure provide a reconstruction error of the order of 11% for the nebula with magnitude 15, thus comparable with the error provided

by the exact PSFs. This result indicates that also very faint stars can be used for a satisfactory PSF estimation.

7. Blind or myopic deconvolution

The results outlined in the previous section imply that if a well-isolated star is available in the FoV, in the sense that the surrounding objects do not perturb significantly its image in a domain a bit broader than that of AO correction, then sufficiently accurate estimates of the PSFs are obtainable leading to satisfactory reconstructions of the scientific target. Unfortunately such a lucky situation can hardly occur, due to the limited angular size of the FoV.

If no star is available in the FoV or if the images of one star in the FoV are perturbed by the images of the surrounding objects (including the object which is the scientific target of the observation), then one does not have sufficient information on the PSFs. In such a case one must consider methods of *blind* (no information) or *myopic* (partial information) deconvolution.

In the case of LN imaging, blind deconvolution can be formulated as the problem of simultaneous minimization of the data-fidelity function, defined in equation (5), with respect to \mathbf{f} and all the PSFs \mathbf{K}_j (defining the matrices A_j). This function is convex and coercive when restricted to each one of these unknown nonnegative variables, but is not convex in all the variables. A crucial remark is that this problem is strictly related to the problem of *nonnegative matrix factorization*, which has important applications in imaging science and in learning theory [44]. This problem is investigated in [45, 46], where two alternating iterative algorithms are given and their convergence is proved. One of these algorithms can be applied to the LN problem and can be briefly described as follows: given the object $\mathbf{f}^{(k)}$ and the PSFs $\mathbf{K}_j^{(k)}$ ($j = 1, \dots, p$) at iteration number k , update the object using one multiple-image RL iteration, with the given PSFs, and, thanks to the symmetry of the convolution product with respect to the exchange of object and PSF, update the PSFs using a single-image RL iteration for each of them (with the given object playing the role of a PSF). Obviously the algorithm is slowly convergent and early stopping is required because the problem is ill-posed.

Another approach consists in the alternating minimization method: at each iteration, the objective function is minimized with respect to one variable with the other fixed at the values provided by the previous iteration. Convergence is proved in [33]. This approach introduces the so-called *iterative blind deconvolution methods*, proposed by several authors for blind deconvolution. Indeed, each minimization problem can also be solved iteratively and iterations must be stopped, so that we have two kinds of iterations: *internal* (inside each minimization problem) and *external* (numbering the minimization problems) iterations. Convergence of the approach for arbitrary numbers of internal iterations is given in [18]. The case of myopic deconvolution corresponds to the situation where one has estimates of the PSFs for initializing the iterations.

This approach is essentially that used in [26] where external iterations are called *cycles*. One cycle updates both the object and the PSFs. However, it is important to remark that for obtaining satisfactory results, other constraints on the PSFs, besides nonnegativity, must be introduced. In the case of p images, inside each cycle one must solve approximately $p + 1$ minimization problem. The first is that providing the update of the object with the PSFs provided by the previous cycle. To this purpose the OSEM algorithm is used with a fixed number of iterations. As concerns the PSFs, the additional constraint on the (known) band of each PSF is introduced; then, RL is used and band-constraint and nonnegativity are imposed at each iteration by a suitable filtering. At the end of the iterations, the result is

re-normalized to the unit ℓ_1 norm. The number of OSEM iterations and of RL iterations are important parameters to obtain satisfactory results. We refer to [26] for a discussion.

Even if this approach is very empirical and must be revisited using recent results on nonnegative matrix factorization, its value consists in demonstrating that additional constraints on the PSFs are crucial for obtaining improved estimates. Another constraint that has been recently proposed in the case of single image blind deconvolution [27], consists in requiring, at the end of each cycle, that the estimated PSF has the correct SR value, since this is a parameter which, in general, is known to the astronomers. An extension to the problem of LN imaging could provide interesting results.

8. Concluding remarks and open problems

In this review, we have described the state of the art of the methods proposed and implemented for reconstructing the images of the LN interferometer for LBT. A demonstration of the performance of these methods has been given on synthetic images only, because real images are not yet available. In our opinion, the proposed methods can already be adequate for the reconstruction of the first LN images, even if some extension could be desirable for the reasons indicated in the following. Therefore, the rest of this section is devoted to a discussion of the problems that, at the present state of our knowledge, should be considered in the next years. We give a list of these problems.

- (i) In this review, we assume that image formation can be modeled in terms of a space-invariant PSF, changing from image to image according to the orientation of the baseline and the AO correction. This assumption is reasonable in the case of multi-conjugate AO correction that will be available for LN. However, in a preliminary stage of operation of the interferometer, variation of the PSFs over the FoV will be possible and, in any case, an exactly uniform AO correction is never reached. Therefore, deconvolution with space-variant PSFs must be considered.

It is obvious that the first issue is to estimate the variation of the PSFs over the field by looking at the stars available in the FoV. When this problem has been solved (using, for instance, the method outlined in section 3.2) the image reconstruction can be performed by considering an image domain decomposition such that, in each domain, the PSFs can be considered as space-invariant and by reconstructing each domain with the methods for boundary effect correction described in section 5.3. Obviously, it may be convenient to consider partially overlapping domains and extract from these non-overlapping domains to obtain the reconstructed image as a mosaic of them.

- (ii) The regularization of the data-fidelity function of equation (5) is an important issue. Until now, regularization has been investigated only in terms of the regularization functions given in section 4.2 and numerical simulations demonstrate that these are adequate for the reconstruction of ‘simple’ astronomical objects such as open star clusters, nebulae, distant galaxies, planetary surfaces, etc. For more complex objects, it should be necessary to investigate the application of methods derived from the regularization in terms of sparse representation of the object with respect to a suitable basis or frame. Examples of applications of these methods to astronomical imaging are given, for instance, in [58, 59]. Another important problem, already mentioned in section 6.1.6, is the reconstruction of objects consisting of bright stars superimposed to diffuse and faint objects.
- (iii) The iterative methods investigated in this review are in general slow, except in the case of faint objects, hence high Poisson noise. But, for sufficiently bright objects, they may require thousands of iterations and, in the case of images with the maximum size of

2048 × 2048 pixels, this can mean hours of computation. Acceleration methods have been briefly described in this review but, in general, they are not completely satisfactory, both because no convergence proof is available and because in some critical cases they do not provide satisfactory results (a practical consequence of the lack of a rigorous mathematical analysis). Therefore, sound and efficient acceleration of the proposed algorithms is essentially an open issue. Investigation of the application of SGP [17] to the multiple-image RL algorithm is in progress, as well as its implementation on GPUs. The methods proposed in [19, 20] should also be considered.

- (iv) Finally, blind deconvolution is an interesting and basic problem. The methods proposed until now clarify the importance of specific physical constraints on the PSFs, such as band-limiting, SR, etc, in addition to non-negativity. The recent interest in the problem of nonnegative matrix factorization can lead to a sound mathematical analysis and to efficient reconstruction algorithms.

The previous list is certainly not complete. This is what we believe will be important. But certainly other important and interesting problems will arise when it is possible to process real images of the interferometer.

Acknowledgments

This work was partially supported by MUR (Italian Ministry for University and Research) grant 2006018748. We thank Carmelo Arcidiacono of the Astronomical Observatory of Bologna for kindly providing both the simulated AO corrected PSFs and the infrared image of Io used for deriving the model of the planetary surface.

References

- [1] Anconelli B, Bertero M, Boccacci P, Carbillet M, Lantéri H and Correia S 2004 Deconvolution methods for LINC-NIRVANA data reduction *Proc. SPIE* **5491** 932–43
- [2] Anconelli B, Bertero M, Boccacci P, Carbillet M and Lantéri H 2005 Restoration of interferometric images: III. Efficient Richardson–Lucy methods for LINC-NIRVANA data reduction *Astron. Astrophys.* **430** 731–8
- [3] Anconelli B, Bertero M, Boccacci P and Carbillet M 2005 Restoration of interferometric images: IV. An algorithm for super-resolution of stellar systems *Astron. Astrophys.* **431** 747–55
- [4] Anconelli B, Bertero M, Boccacci P, Carbillet M and Lantéri H 2006 Reduction of boundary effects in multiple image deconvolution with an application to LBT LINC-NIRVANA *Astron. Astrophys.* **448** 1217–24
- [5] Anconelli B, Bertero M, Boccacci P, Desiderà G, Carbillet M and Lantéri H 2006 Deconvolution of multiple images with high dynamic range and an application to LBT LINC-NIRVANA *Astron. Astrophys.* **460** 349–65
- [6] Anscombe F J 1948 The transformation of Poisson, binomial and negative-binomial data *Biometrika* **35** 246–54 (available at <http://www.jstor.org/stable/2332343>)
- [7] Arcidiacono C, Diolaiti E, Tordi M, Ragazzoni R, Farinato J, Vernet E and Marchetti E 2004 Layer-oriented simulation tool *Appl. Opt.* **43** 4288–302
- [8] Bardsley J M and Goldes J 2009 Regularization parameter selection methods for ill-posed Poisson maximum likelihood estimation *Inverse Problems* **25** 095005
- [9] Barrett H H and Meyers K J 2003 *Foundations of Image Science* (New York: Wiley) pp 1047–8
- [10] Bertero M and Boccacci P 2000 Application of the OS-EM method to the restoration of LBT images *Astron. Astrophys. Suppl. Ser.* **144** 181–6
- [11] Bertero M and Boccacci P 2000 Image restoration methods for the Large Binocular Telescope *Astron. Astrophys. Suppl. Ser.* **147** 323–32
- [12] Bertero M and Boccacci P 2005 A simple method for the reduction of boundary effects in the Richardson–Lucy approach to image deconvolution *Astron. Astrophys.* **437** 369–74
- [13] Bertero M, Boccacci P, Desiderà G and Vicidomini G 2009 Image deblurring with Poisson data: from cells to galaxies *Inverse Problems* **25** 123006
- [14] Bertero M, Boccacci P, Talenti G, Zanella R and Zanni L 2010 A discrepancy principle for Poisson data *Inverse Problems* **26** 10500

- [15] Biggs D S C and Andrews M 1997 Acceleration of iterative image restoration algorithms *Appl. Opt.* **36** 1766–75
- [16] Biggs D S C and Andrews M 1998 Asymmetric iterative blind deconvolution of multi-frame images *Proc. SPIE* **3461** 328–38
- [17] Bonettini S, Zanella R and Zanni L 2009 A scaled gradient projection method for constrained image deblurring *Inverse Problems* **25** 015002
- [18] Bonettini S 2011 Inexact block coordinate descent methods with application to non-negative matrix factorization *IMA J. Numer. Anal.* **31** 1431–52
- [19] Byrne C L 1996 Block-iterative methods for image reconstruction from projections *IEEE Trans. Image Process.* **5** 792–4
- [20] Byrne C 2005 Choosing parameters in block-iterative or ordered subset reconstruction algorithm *IEEE Trans. Image Process.* **14** 321–7
- [21] Carbillet M, Correia S, Boccacci P and Bertero M 2002 Restoration of interferometric images: II. The case-study of the Large Binocular Telescope *Astron. Astrophys.* **387** 744–57
- [22] Charbonnier P, Blanc-Féraud L, Aubert G and Barlaud M 1997 Deterministic edge-preserving regularization in computed imaging *IEEE Trans. Image Process.* **6** 298–311
- [23] Ciliégi P, La Camera A, Arcidiacono C, Bertero M, Boccacci P, Diolaiti E, Foppiani I, Lombini M and Schreiber M 2010 Analysis of LBT LINC-NIRVANA simulated images of galaxies *Proc. SPIE* **7734** 7734–88 (available at http://spiedigitallibrary.org/proceedings/resource/2/psisdg/7734/1/77342G_1?isAuthorized=no)
- [24] Correia S, Carbillet M, Boccacci P, Bertero M and Fini L 2002 Restoration of interferometric images: I. The software package AIRY *Astron. Astrophys.* **387** 733–43
- [25] Csizsár I 1991 Why least squares and maximum entropy? An axiomatic approach to inference for linear inverse problems *Ann. Stat.* **19** 2032–66
- [26] Desiderà G, Anconelli B, Bertero M, Boccacci P and Carbillet M 2006 Application of iterative blind deconvolution to the reconstruction of LBT LINC-NIRVANA images *Astron. Astrophys.* **452** 727–43
- [27] Desiderà G and Carbillet M 2009 Strehl-constrained iterative blind deconvolution for post-adaptive-optics data *Astron. Astrophys.* **507** 1759–62
- [28] Donoho D L, Johnstone I M, Hoch J C and Stern A S 1992 Maximum entropy and the nearly black object *J. R. Stat. Soc. B* **54** 41–81 (available at <http://www.ams.org/mathscinet/search/publdoc.html?pg1=MR&r=1&s1=MR1157714&vfpref=html>)
- [29] Esposito S *et al* 2010 First light AO (FLAO) system for LBT: final integration, acceptance test in Europe, and preliminary on-sky commissioning results *Proc. SPIE* **7736** 773609
- [30] Geman S and Geman D 1984 Stochastic relaxation, Gibbs distributions, and the Bayesian restoration of images *IEEE Trans. Pattern Anal. Mach. Intell.* **6** 721–41
- [31] Geman S and McClure D 1987 Statistical methods for tomographic image reconstruction *Bull. Int. Stat. Inst.* **LII-4** 5–21 (available at <http://www.ams.org/mathscinet/search/publdoc.html?pg1=MR&r=1&s1=MR1027188&vfpref=html>)
- [32] Green P J 1990 Bayesian reconstructions from emission tomography data using a modified EM algorithm *IEEE Trans. Med. Imaging* **9** 84–93
- [33] Grippo L and Sciandrone M 2000 On the convergence of the block nonlinear Gauss–Seidel method under convex constraints *Oper. Res. Lett.* **27** 127–36
- [34] Hege E K, Christou J, Cheselka M and Jefferies S M 1999 Aperture synthesis imaging with Large Binocular Telescope *ASP Conf. Ser.* **174** 33–9 (available at <http://adsabs.harvard.edu/abs/1999ASPC..174...33H>)
- [35] Hege E K, Christou J, Jefferies S M and Cheselka M 1999 Technique for combining incoherent interferometric images *J. Opt. Soc. Am. A* **16** 1745–50
- [36] Herbst T *et al* 2003 LINC-NIRVANA: a Fizeau beam combiner for the large binocular telescope *Proc. SPIE* **4838** 456–65
- [37] Hofmann K H, Driebe T, Heininger M, Scertl D and Weigelt G 2005 Reconstruction of aperture synthesis images from LBT LINC-NIRVANA data using the Richardson–Lucy and space-variant building block method *Astron. Astrophys.* **444** 983–93
- [38] Hudson H M and Larkin R S 1994 Accelerated image reconstruction using ordered subsets of projected data *IEEE Trans. Med. Imaging* **13** 601–9
- [39] Iusem A N 1991 Convergence analysis for a multiplicatively relaxed EM algorithm *Math. Methods Appl. Sci.* **14** 573–93
- [40] Kaipio J and Somersalo E 2005 *Statistical and Computational Inverse Problems* (Berlin: Springer)
- [41] La Camera A, Desiderà G, Arcidiacono C, Boccacci P and Bertero M 2007 Advances in the reconstruction of LBT LINC-NIRVANA images *Astron. Astrophys.* **471** 1091–7

- [42] Lantéri H, Roche M, Cuevas O and Aime C 2001 A general method to devise maximum-likelihood signal restoration multiplicative algorithms with nonnegativity constraints *Signal Process.* **81** 945–74
- [43] Lantéri H, Roche M and Aime C 2002 Penalized maximum likelihood image restoration with positivity constraints: multiplicative algorithms *Inverse Problems* **18** 1397–419
- [44] Lee D D and Seung H S 1999 Learning the parts of objects by non-negative matrix factorization *Nature* **401** 788–91
- [45] Lee D D and Seung H S 2000 Algorithms for nonnegative matrix factorization *Adv. Neural Inform. Process.* **13** 556–62 (available at <http://books.nips.cc/papers/files/nips13/LeeSeung.pdf>)
- [46] Lin C-J 2007 On the convergence of multiplicative update algorithms for non-negative matrix factorization *IEEE Trans. Neural Netw.* **18** 1589–96
- [47] Lucy L B 1974 An iterative technique for the rectification of observed distributions *Astron. J.* **79** 745–54
- [48] Natterer F and Wübbeling F 2001 *Mathematical Methods in Image Reconstruction* (Philadelphia, PA: SIAM)
- [49] Ng K M, Chan R H and Tang W-C 1999 A fast algorithm for deblurring models with Neumann boundary conditions *SIAM J. Sci. Comput.* **21** 851–66
- [50] Portilla J, Strela V, Wainwright M J and Simoncelli E P 2003 Image denoising using scale mixtures of Gaussians in the wavelet domain *IEEE Trans. Image Process.* **12** 1338–51
- [51] Ragazzoni R *et al* 2003 A visible MCAO channel for NIRVANA at the LBT *Proc. SPIE* **4839** 536–43
- [52] Richardson W H 1972 Bayesian based iterative method of image restoration *J. Opt. Soc. Am.* **62** 55–9
- [53] Serra Capizzano S 2003 A note on anti-reflective boundary conditions and fast deblurring models *SIAM J. Sci. Comput.* **25** 1307–25
- [54] Shepp L A and Vardi Y 1982 Maximum likelihood reconstruction for emission tomography *Trans. Med. Imaging* **MI-1** 113–22
- [55] Simoncelli E P and Freeman W T 1995 The steerable pyramid: a flexible architecture for multi-scale derivative computation *Proc. IEEE Conf. Image Process.* **3** 444–7
- [56] Snyder D L, Hammoud A M and White R L 1993 Image recovery from data acquired with a charge-coupled-device camera *J. Opt. Soc. Am.* **10** 1014–23
- [57] Snyder D L, Helstrom C W, Lanterman A D, Faisal M and White R L 1994 Compensation for readout noise in CCD images *J. Opt. Soc. Am. A* **12** 272–83 (available at <http://www.opticsinfobase.org/abstract.cfm?id=33107>)
- [58] Starck J-L and Murtagh F 2006 *Astronomical Image and Data Analysis* (Berlin: Springer)
- [59] Starck J-L, Fadili M J and Murtagh F 2007 The undecimated wavelet decomposition and its reconstruction *IEEE Trans. Image Process.* **16** 297–309
- [60] Veklerov E and Llacer J 1987 Stopping rule for the MLE algorithm based on statistical hypothesis testing *Trans. Med. Imaging* **MI-6** 313–9
- [61] Vio R, Nagy J, Tenorio L and Wamsteker W 2004 A simple but efficient algorithm for multiple image deblurring *Astron. Astrophys.* **416** 403–10